Single-atom CoN$_4$ sites with elongated bonding induced by phosphorus doping for efficient H$_2$O$_2$ electrosynthesis

Jingjing Liu [a],[1], Zengxi Wei [b],[1], Zhichao Gong [a], Minmin Yan [a], Yongfeng Hu [c], Shuangliang Zhao [b], Gonglan Ye [a],[*], Huilong Fei [a],[*]

[a] State Key Laboratory for Chemo/Biosensing and Chemometrics, Advanced Catalytic Engineering Research Center of the Ministry of Education and College of Chemistry and Chemical Engineering, Hunan University, Changsha 410082, China
[b] Guangxi Key Laboratory of Petrochemical Resource Processing and Process Intensification Technology and School of Chemistry and Chemical Engineering, Guangxi University, Nanning 530004, China
[c] Canadian Light Source, Inc. (CLSI) Saskatoon, Saskatchewan S7N 2V3, Canada

ARTICLE INFO

ABSTRACT

Modification of the microenvironment of metal- and nitrogen-coordinated nanocarbons (M-N-Cs) is critical in regulating their electronic structure and thus catalytic selectivity toward the oxygen reduction reaction (ORR). Introducing heteroatoms into the carbon matrix of M-N-Cs could affect the coordination configuration and charge density of the metal centers, but it has rarely been applied to improve the ORR selectivity for H$_2$O$_2$ electrosynthesis. Here we show that doping phosphorus (P) atoms into the carbon substrate of a Co-N-C catalyst lengthens the Co−N bond, decreases the electron density of the Co, and weakens the adsorption strength of the key *OOH intermediate on the active sites, as demonstrated by both experimental and theoretical results. Consequently, this P-doped Co-N-C catalyst presents outstanding catalytic performance toward the 2e$^-$ ORR with an early onset potential of 0.81 V (vs. the reversible hydrogen electrode), exceptional H$_2$O$_2$ selectivity above 90% in a wide potential range from 0.1 V to 0.7 V (maximum value of ∼ 97% at 0.5 V) and a large turnover frequency (2.36 ± 0.15 s^{-1} at 0.65 V) in alkaline electrolyte, superior to almost all previously reported counterparts. Moreover, an unprecedented H$_2$O$_2$ production rate up to 11.2 $mol_{H_2O_2}g_{catalyst}^{-1}h^{-1}$ with long-term durability (110 h) is obtained when the catalyst is assessed as a gas diffusion layer in a practical flow cell.

1. Introduction

Hydrogen peroxide (H$_2$O$_2$) is crucial for a wide range of applications, including chemical synthesis, paper production, wastewater treatment and medical industries [1–3]. The global H$_2$O$_2$ market is predicted to reach US\$ 4.06 billion in 2027 [4]. At present, H$_2$O$_2$ is obtained at an industrial scale mainly from the anthraquinone-based process that is energy-consuming and environmentally unfriendly [5,6]. To this end, the electrosynthesis of H$_2$O$_2$ via the two-electron (2e$^-$) oxygen reduction reaction (ORR) is an emerging alternative with the merits of on-demand and decentralized production of H$_2$O$_2$ using renewable electricity [7,8]. However, the 2e$^-$ ORR pathway competes with the branching 4e$^-$ pathway during the multi-electron transfer process, calling for the development of selective and active catalysts [9,10]. Noble metals and their alloys (e.g., Pt-Hg) have been identified as the

most effective catalysts, but their high cost and scarcity severely constrain the large-scale application [11–14]. As a result, an increasing number of nonprecious metal catalysts have been explored with considerable improvements in catalytic performances [15–17]. However, it remains a grand challenge to selectively direct the ORR toward either the 2e$^-$ or 4e$^-$ pathway.

The ORR selectivity of a catalyst generally hinges on the absorption behavior (strength and configuration) of the key intermediate *OOH on the active sites, which is strongly affected by the electronic structure (the metal *d* band center) of the catalyst [18–20]. Therefore, catalysts with tunable electronic structure are desirable as they allow for the fine control of the ORR pathways. Single atom catalysts (SACs) have recently been extensively studied for their combined merits of both homogeneous and heterogeneous catalysts [21–24]. Among them, metal- and nitrogen-coordinated nanocarbons (M-N-Cs) with the porphyrin-like

MN$_4$ moieties represent the most promising SACs for electrocatalytic applications [25–28]. More importantly, M-N-Cs offer high degrees of freedom to modulate their electronic structure that is dictated by the coordination environment of the metal sites-[29–32].Particularly, strain engineering is a powerful strategy to tune the coordination environment (e.g., bonding configuration and bond length) and thus catalytic reactivity of M-N-Cs [33–35]. For instance, Han et al. found that tuning the curvature of the carbon substrates could modulate the geometry distortion of the single-atom Cu sites, thereby affecting the charge transferred from Cu to O$_2$ and thus the ORR activity [36]. Qin et al. reported that the introduce of a S anion into the second coordination shell of a RuN$_4$ site could expand the Ru−N bond and increase the electron density around Ru sites, thus boosting the ORR activity [37]. However, the strategy of strain-induced electronic structure tuning has rarely been used to regulate the ORR selectivity toward H$_2$O$_2$ electrosynthesis.

In this work, we report a single-atom Co-N-C catalyst with elongated bonding induced by the doping of phosphorus (P) heteroatoms into the carbon substrate (denoted as CoN$_4$-PC) for highly active and selective 2e$^-$ ORR. Combining various experimental characterizations with density functional theory (DFT) calculations, we find that the introduce of P dopants can stretch the Co−N bond of the CoN$_4$ sites, decrease the electron density of the Co atoms and optimize the *OOH adsorption strength on the active sites of CoN$_4$-PC. As a result, this catalyst delivers an exceptional performance for the 2e$^-$ ORR with an early onset potential of 0.81 V vs. the reversible hydrogen electrode (RHE), high H$_2$O$_2$ selectivity above 90% in a wide potential range from 0.1 V to 0.7 V (maximum value of ~ 97% at 0.5 V), and a large turnover frequency (TOF) (2.36 $\pm$ 0.15 s^{-1} at 0.65 V) in 0.1 M KOH, making it superior to almost all previously reported SACs for H$_2$O$_2$ electrosynthesis. Moreover, when evaluated in a practical flow cell, an unprecedent H$_2$O$_2$ production rate of 11.2 $mol_{H_2o_2}g_{catalyst}^{-1}h^{-1}$was achieved during a 110-h long-term durability test.

2. Experimental section

2.1. Synthesis of CoN$_4$-PC

CoN$_4$-PC was synthesized via a polymerization-and-pyrolysis strategy. Specifically, phytic acid (1 mmol) and 2 mL 3.6 mg mL^{-1} aqueous solution of CoCl$_2$·6 H$_2$O (0.031 mmol) were mixed with aniline monomer (5 mmol) by sonication. After being cooled to 4 ℃, 1 mL 286 mg mL^{-1} ammonium persulfate ((NH$_4$)$_2$S$_2$O$_8$) solution (1.25 mmol) was quickly added to the above mixture and sonicated for 1 min to form a dark-green hydrogel. The resultant hydrogel was aged at room temperature for 12 h and then lyophilized to obtain an aerogel, which was then calcined at 900 ℃ for 1 h in a tubular furnace under a constant flow of Ar (300 sccm) with a heating rate of 5 ℃ min^{-1} to obtain CoN$_4$-PC. For comparison, control samples of CoN$_4$-C and N-PC were prepared following the similar procedure except that no phytic acid or cobalt precursor were added, respectively.

2.2. Electrocatalytic ORR performance evaluated with RRDE technique

The electrochemical measurements were carried out in O$_2$-saturated 0.1 M KOH electrolyte within a three-electrode system at room temperature on a CHI 760E electrochemical workstation (Shanghai, Chenhua). A Teflon cell was used to avoid contamination from glass components. The ORR activity and selectivity were studied by linear sweep voltammetry (LSV) using a rotating ring-disk electrode (RRDE) (Pine Instruments Corporation). The disk electrode was scanned at a rate of 10 mV s^{-1} at 1600 rpm, and the Pt ring electrode potential was fixed at 1.2 V vs. RHE. A glassy carbon electrode loaded with catalysts was used as the working electrode, while graphite rod and Hg/HgO (1 M KOH) electrode were used as the counter electrode and reference

electrode, respectively. To prepare the working electrode, 2 mg catalyst was added into the mixture of 480 μL ethanol and 20 μL Nafion (5 wt%) and sonicated for 1 h to form a homogeneous suspension. Then, 2.5 μL of the above suspension was dropped on the glassy carbon core (area: 0.196 cm^{-2}) of the RRDE to achieve a catalyst loading of 50 μg cm^{-2}. All potentials were converted to RHE scale by $E_{RHE} = E_{Hg/HgO} + 0.901$ based on the calibration result (Fig. S1) and corrected with 95% iR compensation. Before the H$_2$O$_2$ detection, scans of cycle voltammetry (~ 20 cycles) from − 0.05 to - 0.40 V vs. RHE were carried out on the Pt ring electrode of the RRDE to electrochemically clean it. The applied disk voltage was fixed at 0.5 V in the chronoamperometry test and the fresh electrolyte was replaced every 2 h during the durability test.

The H$_2$O$_2$ selectivity (%) and electron transfer number (n) were evaluated by the following two equations [31]:

$$H_2O_2\ (\%) = 200 \times \frac{\frac{I_R}{N}}{\frac{I_R}{N} + I_D} \tag{1}$$

$$n = 4 \times \frac{I_D}{I_D + \frac{I_R}{N}} \tag{2}$$

where I_R and I_D are the ring and disk currents, respectively; N is the ring current collection efficiency (calibrated to be 0.238) (Fig. S2).

The kinetic current density for H$_2$O$_2$ production was extracted from the Koutecký-Levich (K-L) equation:

$$\frac{1}{j} = \frac{1}{j_l} + \frac{1}{j_k} \tag{3}$$

where j is the measured ring current density; j_l and j_k are the diffusion limiting current density (defined at the potential of 0.2 V) and kinetic current density of the ring electrode, respectively.

The turnover frequency (TOF) was determined as follows [27,31]:

$$TOF(s^{-1}) = \frac{\text{turnover number of O}_2\,\text{molecules}}{\text{number of active sites}}$$
$$= \frac{j_{H_2O_2} \times M_{metal}}{n \times F \times m_{catalyst} \times \omega_{metal}} \tag{4}$$

where $j_{H_2O_2}$ is the current density (A cm^{-2}) for H$_2$O$_2$ production measured from the Pt ring electrode and corrected with the collection efficiency at a given potential, M_{metal} is the atomic weight of the metal (g mol^{-1}, here the M_{Co} is 58.93 g mol^{-1}), n is the number of electrons transferred during H$_2$O$_2$ production process ($n = 2$), F is the Faraday constant (96485 C mol^{-1}), $m_{catalyst}$ is the catalyst loading on the disk electrode (g cm^{-2}, here the $m_{catalyst}$ is 5×10^{-5} g cm^{-2}) and ω_{metal} is the metal weight fraction in the catalyst (wt%, here ω_{Co} is 0.5 wt%). As a result, the TOF (s^{-1}) for the H$_2$O$_2$ production of CoN$_4$-PC is calculated to be 2.36 $\pm$ 0.15 (s^{-1}) at 0.65 V.

2.3. Electrocatalytic H$_2$O$_2$ production evaluated with a flow cell

Bulk H$_2$O$_2$ production was performed in a two-compartment flow cell (Shanghai Chuxi Industrial Co., Ltd) with a three-electrode configuration. The cathode is a Teflon-treated gas diffusion layer (GDL, working area: 1 cm^2) coated with the CoN$_4$-PC catalyst at loading of 0.1 mg cm^{-2}, and the anode is a Ni foam (area: 4 cm^2, thickness:1 mm). The cathode and anode are separated by an anion exchange membrane (area: 1 cm^2, FAA-3PK-130, Fumasep). A pre-calibrated Hg/HgO (E_{RHE} = E$_{Hg/HgO}$ + 0.919, Fig. S3) was used as the reference electrode and placed close to the working electrode in the cathode chamber. The cathode compartment (backside of the GDL) was fed with continuous O$_2$ at a rate of 10 sccm and the fresh electrolyte was pumped into the cathode chamber with a flow rate of 172 mL h^{-1}. The discharge polarization curves were obtained with the linear sweep voltammetry method in 0 – 0.9 V (10 mV s^{-1}) and the H$_2$O$_2$ production rate as well as the long-term chronoamperometry stability test were performed at a fixed potential of 0.3 V in 1.0 M KOH.

The H_2O_2 concentration in the flow cell was measured by the Ce^{4+} titration method [31]. As the yellow-colored Ce^{4+} is converted to the colorless Ce^{3+} in the presence of H_2O_2 according to the reaction: $2Ce^{4+} + H_2O_2 \rightarrow 2Ce^{3+} + 2H^+ + O_2$, the H_2O_2 concentration can be calculated from the following relationship: $C_{H_2O_2} = \frac{1}{2}\Delta C_{Ce^{4+}}$. Prior to measurement, 0.25 mM $Ce(SO_4)_2$ was firstly dissolved in 0.5 M H_2SO_4 solution, and then various volumes of 0.1 wt% H_2O_2 (0, 5, 10, 15 and 20 μL) were added to the 6 mL $Ce(SO_4)_2$ solution to obtain the calibration curves (Fig. S4) between absorbance and H_2O_2 volumes tested by UV–vis spectrophotometry (200 – 600 nm). After electrolysis for a period of time, 50 μL of the cathode electrolyte was neutralized with 0.5 M H_2SO_4 and then added to the standard Ce^{4+} solution. The Faradaic efficiency

(FE) for H_2O_2 production can be calculated using the following equation [2]:

$$FE_{H_2O_2}\ (\%) = \frac{C_{titration}}{C_{theory}} \times 100 = \frac{2 \times n_{H_2O_2} \times F \times V}{J} \times 100 \quad (5)$$

where $n_{H_2O_2}$ represents the H_2O_2 concentration (mol L^{-1}) in electrolyte, F is the Faraday constant (96,485 C mol^{-1}), v is the electrolyte flow rate (mL s^{-1}), J indicates the current applied (mA).

Additional experimental details about the reagents and chemicals, material characterizations and degradation experiment of organic dyes as well as theoretical calculations were included in the Supporting Information.
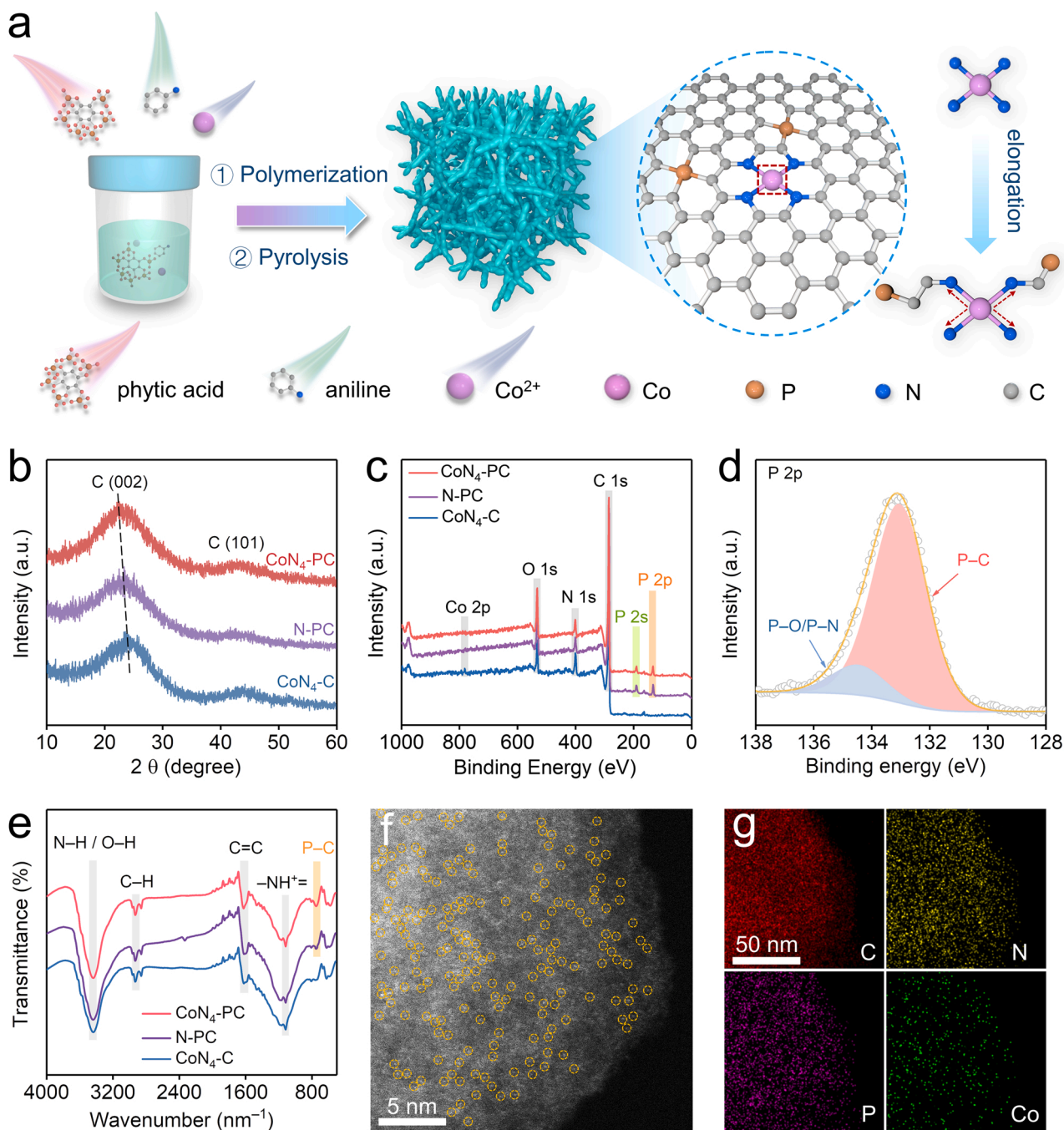

Fig. 1. Characterization of structure and composition. (a) Schematic diagram for the preparation of CoN_4-PC. (b) XRD patterns of CoN_4-PC, N-PC and CoN_4-C. (c) XPS survey spectra of CoN_4-PC, N-PC and CoN_4-C. (d) High-resolution P 2p XPS spectrum of CoN_4-PC. (e) FT-IR spectra of CoN_4-PC, N-PC and CoN_4-C. (f) ADF-STEM image of CoN_4-PC showing the uniform distribution of Co atoms. (g) EDS elemental mapping of C, N, P and Co in CoN_4-PC.

3. Results and discussion

3.1. Synthesis and structural characterization

CoN4-PC was synthesized on a gram-scale approach consisting of two-step polymerization and pyrolysis treatments (Figs. 1a and S5). Briefly, aniline monomers were polymerized into polyaniline network in the presence of phytic acid and controlled amounts of cobalt precursor (CoCl2·6 H2O). The resultant composite in the form of aerogel was then pyrolyzed under inert atmosphere at 900 ℃ for 1 h to obtain CoN4-PC. The detailed preparation process was described in the Experimental section. Control samples of CoN4-C (without P dopants) and metal-free N-PC were prepared via the similar process but without the addition of phytic acid and cobalt salt, respectively. It is noteworthy that NiN4-PC and FeN4-PC could be prepared via the similar process of CoN4-PC by replacing metal precursors from Co to Ni and Fe (Figs. S6 and S7), suggesting that the polymerization-and-pyrolysis method is universal for preparing different types of P-modified M-N-Cs.

The structure and composition of CoN4-PC, CoN4-C and N-PC were characterized by various techniques, as shown in Fig. 1. Powder X-ray diffraction (XRD) patterns reveal that all three samples display two broad peaks at $\sim 26°$ and $\sim 44°$ (Fig. 1b), suggesting that the carbon substrates are of low crystallinity. No signals attributed to crystalline Co metals were detected. Notably, negative shifts in the (002) peak were observed when P atoms were incorporated into the carbon substrates, indicating that the P atoms with larger radius can expand the carbon layer spacing and alleviate the stacking of carbon layers [38–40]. X-ray photoelectron spectroscopy (XPS) survey spectra in Fig. 1c reveal the presence of C, N and O elements in all three samples, but additional peaks assigned to P atoms were identified in CoN4-PC and N-PC, indicating the successful P doping into the carbon matrix. No obvious signals of Co 2p were observed due to the ultrasmall Co content. The elemental compositions of these three samples determined by XPS were summarized in Table S1, showing that the contents of P are 2.94 at% and 2.28 at% for CoN4-PC and N-PC, respectively. Similar to that of N-PC (Fig. S8), the high-resolution P 2p spectrum of CoN4-PC can be deconvoluted into P − C (133.0 eV) and P − O/P − N (134.4 eV) species, and no P − Co species (~ 129 eV) were identified (Fig. 1d) [41,42]. In addition, the high-resolution C 1 s spectrum of CoN4-PC can be deconvoluted into C═C (284.8 eV), C−P (286.1 eV), C−N (287.2 eV), O−C═O (288.4 eV), and $\pi − \pi$ * transition (289.7 eV) (Fig. S9) [43].

The P doping into the carbon matrix in CoN4-PC and N-PC was further confirmed by the Fourier-transform infrared spectra (FT-IR) (Fig. 1e), which display obvious P − C stretching vibration peaks [44]. N2 adsorption/desorption curves of CoN4-PC and N-PC both show typical type-I isotherms with a steep uptake at a low relative pressure (Fig. S10), suggesting the abundance in micropores (Fig. S11) [45,46]. The specific surface area (SSA) of CoN4-PC and N-PC were determined to be 605 m² g⁻¹ and 622 m² g⁻¹, respectively, almost six times that of CoN4-C (101 m² g⁻¹) (Table S2), due to the inclusion of phytic acid as the precursor for preparing CoN4-PC and N-PC, serving as blowing agent that generates volatile species (e.g., CO, PH3) during the pyrolysis step. This was confirmed by the increasing tread in the SSA of samples with the increase in the amounts of phytic acid added for preparing CoN4-PC (Fig. S12). Scanning electron microscopy (SEM) images reveal that CoN4-PC possesses crosslinked and branched carbon nanofibers with diameters of $\sim 100 − 200$ nm (Fig. S13). Transmission electron microscopy (TEM) images display that the carbon matrix is highly disordered and no crystalline Co was observed (Fig. S14). Annular dark-field scanning TEM (ADF-STEM) reveals the uniform distribution of Co atoms (highlighted by orange dashed circles) across the carbon matrix (Fig. 1f). The energy dispersive spectrum (EDS) mapping suggests the homogeneous distribution of C, N, P and Co elements in CoN4-PC (Fig. 1g). The Co loading in CoN4-PC was determined to be 0.50 wt% by the inductively coupled plasma mass spectrometry (ICP-MS) (Table S3).

3.2. Analysis of chemical state and atomic structure

Raman spectra show the disorder-related D band at ~ 1350 cm⁻¹ and graphitization-related G band at ~ 1575 cm⁻¹ (Fig. 2a). The values of I_D-to-I_G ratio are comparable for CoN4-C (1.01), CoN4-PC (1.02) and N-PC (0.99), indicating their similar degree in defects [47]. Notably, the G band of CoN4-PC and N-PC shifts positively by ~ 10 cm⁻¹ compared to CoN4-C, which could be attributed to the electronic structure tuning of the carbon substrate induced by the P doping [48,49]. The carbon K-edge X-ray absorption near edge structure (XANES) spectra of all three samples present three main peaks at ~ 286.3 eV, ~ 288.7 eV and ~ 293.0 eV, assigned to the dipole transition of the aromatic C 1 s core electron into the π * (C═C), π * (C−N/C−P) and σ * (C−C) antibonding states, respectively (Fig. 2b) [43]. The C−N/C−P peaks of CoN4-PC and N-PC shift by ~ 0.3 eV toward higher energy compared to that of CoN4-C, probably attributing to P doping-induced electronic modification of the carbon matrix. Meanwhile, the P L-edge spectra of CoN4-PC and N-PC confirm that the P atoms were successfully doped into carbon substrate without the formation of Co−P bond (Fig. S15). The N K-edge XANES spectra identify four peaks assigned to pyridinic N, pyrrolic N, graphitic N species and the σ * transition of N 1 s to C−N in all samples (Fig. 2c) [50,51]. Compared with that of CoN4-C, the pyridinic N peak for CoN4-PC is weakened in intensity and up-shifted in energy, as a result of P doping. The high-resolution N 1 s XPS spectra of the three samples are deconvoluted into four peaks, including pyridinic N, pyrrolic N, graphitic N, and oxidized N (Fig. 2d). Notably, the intensity of pyridinic N peak for CoN4-PC decreases significantly compared to that of CoN4-C (Figs. 2d and S16), in line with the N K-edge XANES results.

The electronic structure and coordination configurations of Co sites were investigated by hard XANES and extended X-ray absorption fine structure (EXAFS). As shown in Fig. 2e, the adsorption energy of Co K-edge XANES for CoN4-PC and CoN4-C situates between Co foil and CoO, implying that the oxidation state of Co in these two samples is between 0 and + 2. Compared to CoN4-C, CoN4-PC displays a stronger and sharper white-line peak that is related to 1 s → 4p transitions, indicating more electron transfer from Co to the coordinators in CoN4-PC [52]. This result is confirmed by the higher oxidation state of Co (+1.55) in CoN4-PC than that (+1.30) of CoN4-C, determined by the first derivative of Co K-edge XANES (inset of Fig. 2e and Fig. S17), and the higher binding energy of the Co 2p$_{3/2}$ XPS peak of CoN4-PC compared to that of CoN4-C (Fig. S18) [53]. For the Fourier transformed EXAFS (FT-EXAFS) spectra (Fig. 2 f), no Co−Co peak at ~ 2.18 Å was identified in CoN4-C and CoN4-PC, suggesting the absence of crystalline Co. A major peak at ~ 1.42 Å that corresponds to the Co–N backscattering was observed in CoN4-C and it shifts by ~ 0.1 Å toward larger R value in CoN4-PC [24]. Wavelet transform EXAFS (WT-EXAFS) spectra manifest that only one maximum intensity at ~ 5.0 Å⁻¹ in k space (Fig. 2 g), confirming the atomic dispersion of Co in CoN4-PC and CoN4-C. The coordination configurations for the CoN$_x$ moieties were determined by the quantitative least-squares EXAFS curve-fitting analyses (Fig. S19 and Table S4). The results suggest that the average number of the coordinated N in the first coordination shell of Co is ~ 4.1 at a distance of 1.94 Å for CoN4-C. In comparison, CoN4-PC has a similar first-shell coordination number ($\sim$ 4.4), but its Co−N bond (1.99 Å) is elongated by ~ 2.6%, indicating the existence of tensile strain resulted from the P-doping effect (Fig. 2 h). Taken together, the Co sites in CoN4-PC and CoN4-C are atomically dispersed and the introduction of P dopants into the carbon matrix could modify the microenvironment of CoN4-PC in terms of the Co valance state and Co–N bond length.

3.3. Electrocatalytic H2O2 production

The ORR electrocatalytic performances of CoN4-PC, N-PC and CoN4-C were firstly assessed by the rotating ring disk electrode (RRDE) technique with a typical three-electrode system in O2-saturated 0.1 M KOH. Prior to test, the H2O2 collection efficiency of the RRDE and the potential
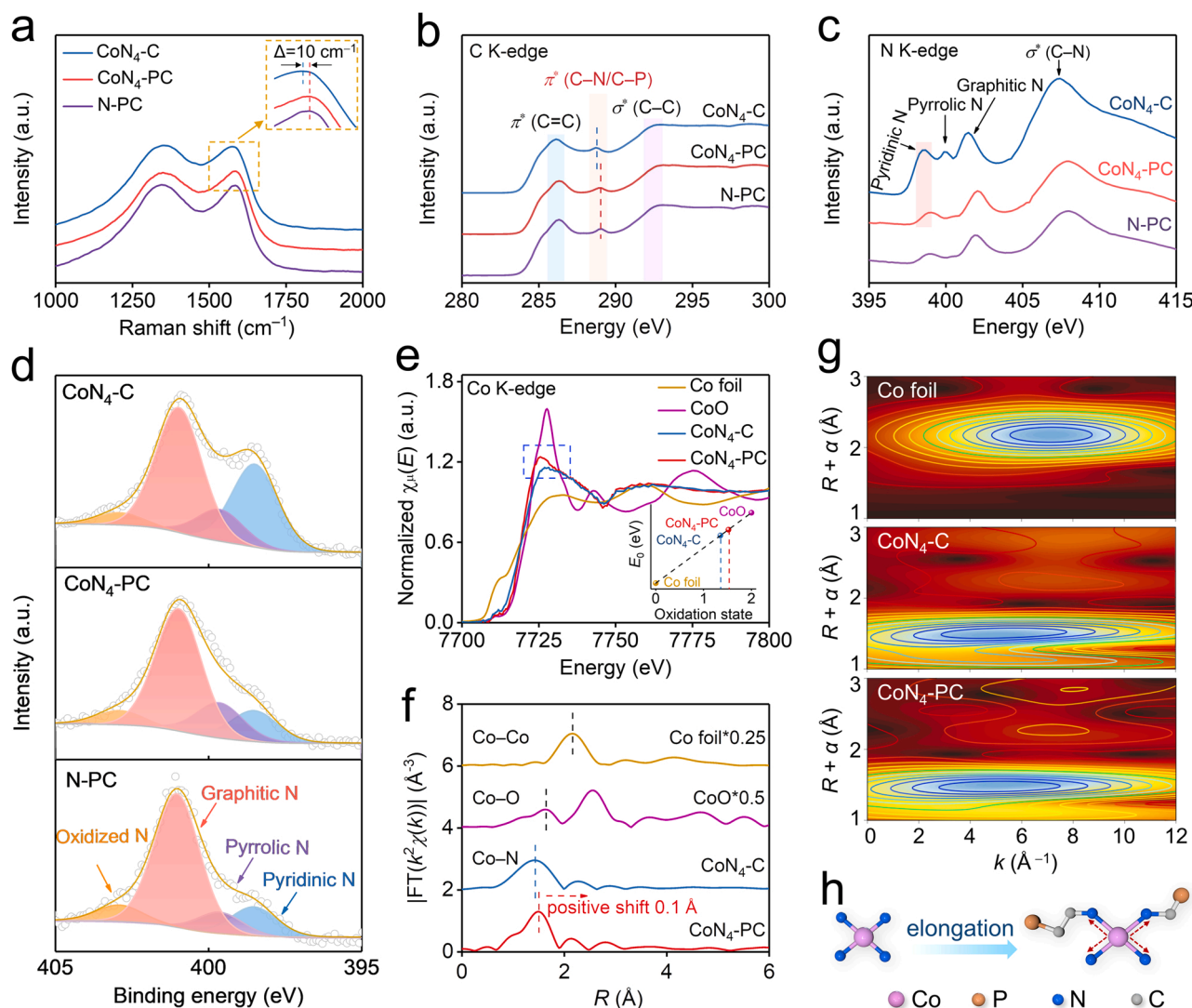
Fig. 2. Analysis of chemical state and atomic structure. (a) Raman spectra of CoN$_4$-C, CoN$_4$-PC and N-PC. The inset shows the enlarged view of the G band. (b) C K-edge and (c) N K-edge XANES spectra of CoN$_4$-C, CoN$_4$-PC and N-PC. (d) High-resolution N 1 s XPS spectra of CoN$_4$-C, CoN$_4$-PC and N-PC. (e) Co K-edge XANES spectra and (f) FT k^2-weighted EXAFS spectra of CoN$_4$-C, CoN$_4$-PC, Co foil and CoO. The inset in (e) shows the fitted valence of Co derived from the XANES spectra. (g) WT k^2-weighted Co K-edge EXAFS spectra of CoN$_4$-C, CoN$_4$-PC and Co foil. (h) Schematic illustration of the Co−N bond length changes before and after the introduce of P dopants.

of the reference electrode were calibrated (Figs. S1 and S2). It should be noted that the performance of CoN$_4$-PC has been optimized by varying the synthetic conditions, including the added amounts of phytic acid, the cobalt contents and the pyrolysis temperature and time (Figs. S20-S24). The catalysts loadings on the electrode were optimized to be 50 μg cm^{-2} (Figs. S25 and S26). Linear sweep voltammetry (LSV) curves presented in Fig. 3a show the similar onset potential (determined at j_{ring} = 0.1 mA cm^{-2}) for the optimized CoN$_4$-PC (0.81 V) and CoN$_4$-C (0.83 V), much more positive than N-PC (0.73 V), suggesting the critical role of Co atoms in enhancing the ORR activity. CoN$_4$-PC delivers a much higher ring current density than CoN$_4$-C in the entire potential region. For instance, the H$_2$O$_2$ production current density at 0.65 V of CoN$_4$-PC (1.92 mA cm^{-2}) is about twice as high as CoN$_4$-C (0.99 mA cm^{-2}) (Fig. 3b). Moreover, CoN$_4$-PC possesses exceptional H$_2$O$_2$ selectivity above 90% in a wide potential range from 0.1 V to 0.7 V (maximum value of ~ 97% at 0.5 V) (Fig. 3c), which far exceeds CoN$_4$-C (~ 60%). Accordingly, the electron transfer numbers (*n*) were calculated to be ~ 2 and ~ 3 for CoN$_4$-PC and CoN$_4$-C, respectively (Fig. S27). The H$_2$O$_2$ reduction reaction experiments showed that CoN$_4$-PC delivered a much lower H$_2$O$_2$ reduction current than CoN$_4$-C (Fig. S28), suggesting that

the high H$_2$O$_2$ selectivity of CoN$_4$-PC originates from its poor activity toward the further reduction of H$_2$O$_2$ to H$_2$O. From the Tafel plots in Fig. 3d, the Tafel slope of CoN$_4$-PC is 50.1 mV dec^{-1}, lower than CoN$_4$-C (74.9 mV dec^{-1}) and N-PC (83.3 mV dec^{-1}), indicating that CoN$_4$-PC possesses faster reaction kinetics for H$_2$O$_2$ production. Further, CoN$_4$-PC displays an exceptional kinetic current density of 5.66 mA cm^{-2} at 0.65 V, much higher than CoN$_4$-C (1.08 mA cm^{-2}) and N-PC (0.76 mA cm^{-2}). To deconvolute the contribution of surface area and intrinsic activity to the apparent activity, the kinetic current density was normalized by the electrochemical active surface area (ECSA) (j_k^{ECSA}). The value of j_k^{ECSA} was determined to be higher for CoN$_4$-PC (0.05 mA cm^{-2}) compared to CoN$_4$-C (0.039 mA cm^{-2}) (Fig. S29). In addition, the TOF value was determined as 2.36 ± 0.15 s^{-1} for CoN$_4$-PC, 2.2-fold higher than CoN$_4$-C (0.75 ± 0.05 s^{-1}), suggesting the higher intrinsic activity of CoN$_4$-PC. The as-presented H$_2$O$_2$ selectivity and TOF of CoN$_4$-PC make it superior to most other 2e$^-$ ORR SACs reported so far in the alkaline testing condition (Fig. 3e and Table S5). Moreover, no obvious attenuations in the activity and selectivity of CoN$_4$-PC were observed after the 10-h chronoamperometry test (Fig. 3 f), and 10,000 scans of cyclic voltammetry (CV) measurements (Fig. S30). Testing
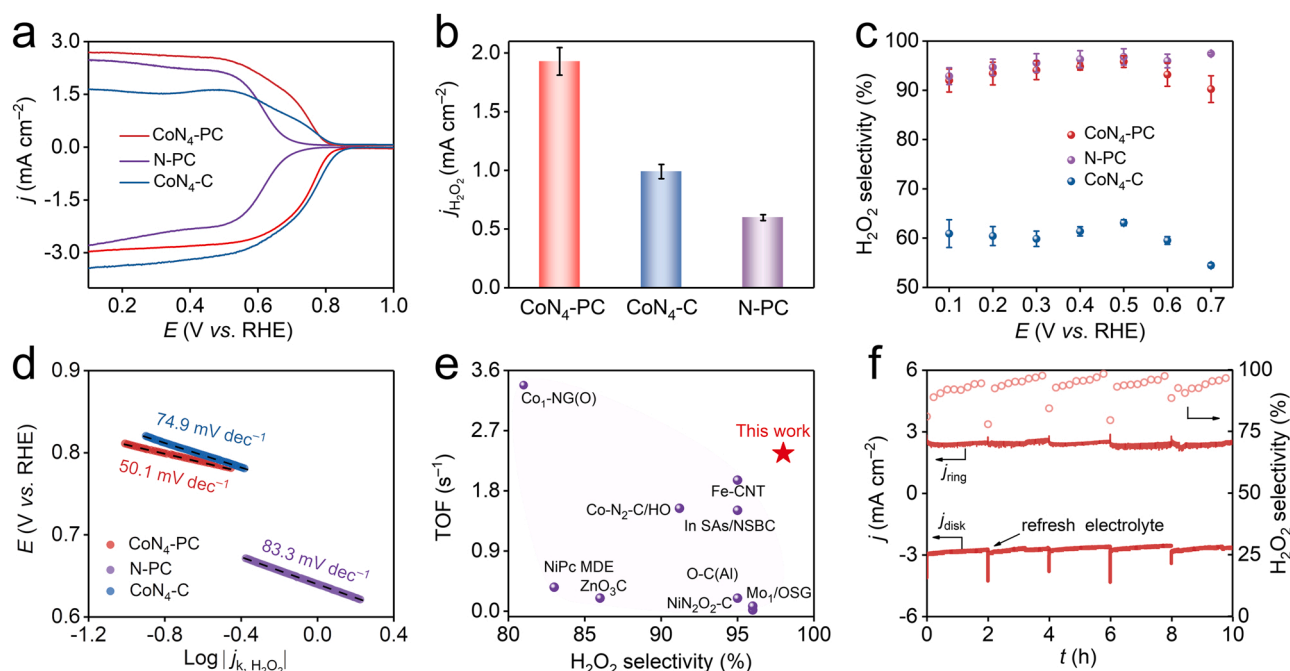
Fig. 3. Electrocatalytic ORR performance evaluated with RRDE. (a) LSV curves of CoN$_4$-PC, N-PC and CoN$_4$-C at 1600 rpm. Scan rate: 10 mV s^{-1}; catalyst loading: 50 μg cm^{-2}. (b) Comparison of H$_2$O$_2$ current density at 0.65 V for CoN$_4$-PC, CoN$_4$-C and N-PC. Error bars indicate standard error from three independent samples. (c) The H$_2$O$_2$ selectivity as a function of the applied potential. (d) Tafel plots of CoN$_4$-PC, N-PC and CoN$_4$-C. (e) ORR performance map in terms of TOF at 0.65 V and maximum H$_2$O$_2$ selectivity for CoN$_4$-PC and the state-of-the-art SACs recently reported in Table S5. (f) The *j-t* curve and H$_2$O$_2$ selectivity of CoN$_4$-PC during the potentiostatic measurement at a fixed disk potential of 0.5 V.

under acidic and neutral media also suggests that CoN$_4$-PC has improved activity and selectivity toward H$_2$O$_2$ electrosynthesis compared to CoN$_4$-C and N-PC (Figs. S31 and S32).

The catalytic performance of CoN$_4$-PC was further evaluated in O$_2$-saturated 1.0 M KOH with a three-electrode flow cell device (Figs. 4a and S33). The working electrode was prepared by coating CoN$_4$-PC on a porous and hydrophobic gas diffusion layer (GDL) [54]. A Ni foam was used as the counter electrode and an anion exchange membrane (AEM) was used to transport anion and restrain substance crossover. The concentration of produced H$_2$O$_2$ was determined by the linear fitting curve (Fig. S4), and the Faradaic efficiency (FE) of CoN$_4$-PC was calculated based on the generated H$_2$O$_2$ concentration and the applied current. The results suggest that CoN$_4$-PC with an optimized catalyst loading of 0.1 mg cm^{-2} exhibits high FE (80% − 92%) in the potential region of 0.7 V − 0.1 V (Figs. 4b and S34). In addition, after 110-h continuous chronoamperometric measurement at 0.3 V, the FE maintains above 75% and the activity as manifested by the current density shows negligible decay, suggesting the catalytic robustness of CoN$_4$-PC (Fig. 4c). Moreover, the average H$_2$O$_2$ production rate was determined to be 11.2 $mol_{H_2O_2} g_{catalyst}^{-1} h^{-1}$, outperforming all SACs for H$_2$O$_2$ electrosynthesis reported to date (Fig. 4d and Table S6). Inspired by the high performance of CoN$_4$-PC, the catholyte after electrolysis was applied to degrade rhodamine B (RhB) organic dye to mimic wastewater treatment via the Fenton reaction, and the change in the concentration of RhB was monitored by UV–vis spectrophotometry [55–58]. As shown in Fig. 4e, after adding 2 mL of the catholyte collected at the cathode compartment with the working electrode kept at a constant potential of 0.25 V for 15 min, the fresh RhB solution (10 mL, 15 mg L^{-1}) was completely degraded (degradation efficiency is up to 98.3%) to be colorless (Figs. S35 and S36, Table S7), suggesting that the generated H$_2$O$_2$ from CoN$_4$-PC can be potentially used to treat wastewater.

3.4. DFT calculations

DFT calculations were performed to unveil the role of P dopants in

affecting the geometric/electronic structure and catalytic behaviors of the CoN$_4$ moieties. We firstly studied various bonding configurations of P dopants in N-doped carbon substrate and calculated the binding energy of P − N/C in each configuration (Figs. S37 and S38). The results show that PC$_4$ configuration possesses the largest binding energy of 7.589 eV and is thus chosen for building the P-modified CoN$_4$ structural models. Further calculations suggest that the introduction of the PC$_4$ sites could lead to the variation in the Co−N bond length of the CoN$_4$ moiety to various degrees depending on the PC$_4$ contents (Fig. 5a), and the optimized structural models (denoted as P$_x$-CoN$_4$ with *x* denoting the number of PC$_4$ sites neighboring the CoN$_4$ moiety) were provided in Fig. S39. Specifically, compared with the CoN$_4$ sites, the mean Co−N bond are elongated by 0.013 Å, 0.024 Å and 0.019 Å in P$_2$-CoN$_4$, P$_3$-CoN$_4$ and P$_4$-CoN$_4$, corresponding to 0.69%, 1.28% and 1.01% tensile strain in the Co−N bond, respectively, corroborating the experimental results. Moreover, it was found that the number of PC$_4$ sites introduced near the CoN$_4$ moiety could affect the adsorption free energy toward the key ORR intermediate *OOH (ΔG_{*OOH}) and thus the 2e$^-$ ORR limiting potential. As shown in Fig. 5b, all investigated P$_x$-CoN$_4$ structures have larger values of ΔG_{*OOH} and higher limiting potentials compared to the bare CoN$_4$ moiety, demonstrating the weaker adsorption strength of *OOH intermediate bonded on these P$_x$-CoN$_4$ moieties and thus resulting in the facile removal of *OOH to form H$_2$O$_2$. Among the different P$_x$-CoN$_4$ configurations, the P$_2$-CoN$_4$ structure was identified as the optimal model catalyst with the highest ORR limiting potential of 0.61 V and its optimized geometry is depicted in Fig. 5c. We also analyzed the relation between the electronic structure and the catalytic activity of the P$_x$-CoN$_4$ catalysts. Fig. S40 displays the calculated charge density difference and Bader charge of Co atoms in the simulated model catalysts with different coverages of P dopants, suggesting that the electronic structure of the Co sites can be effectively regulated by the coverage of P dopants and that the values of Bader charge are in good correlation with the calculated limiting overpotentials (Fig. S41), highlighting the critical role of electronic structure in tuning the catalytic activity.

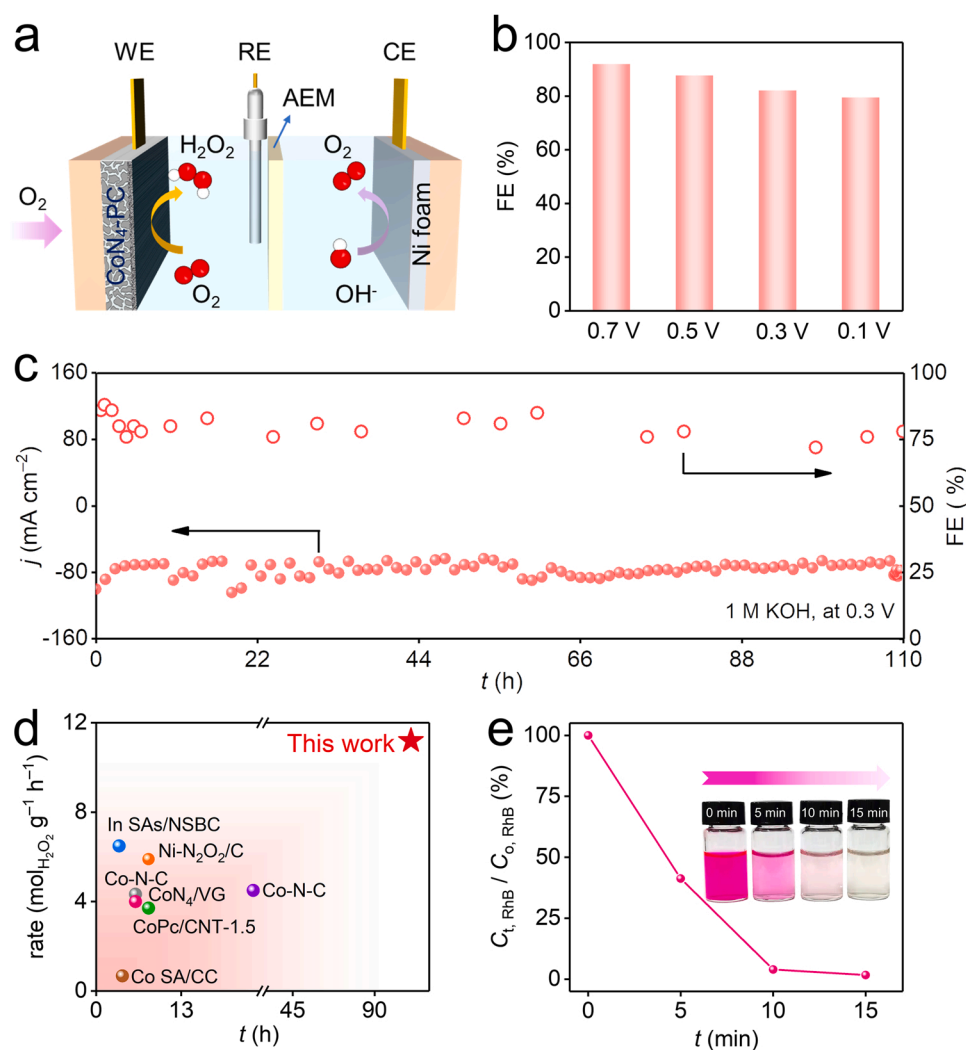The ORR reaction pathways and the free energy diagrams at

Fig. 4. Electrocatalytic ORR performance evaluated with a flow cell. (a) Schematic illustration of the three-electrode flow cell for H_2O_2 electrosynthesis. The flow rate of electrolyte was set at 172 mL h^{-1} and the O_2 feed rate was fixed at 10 sccm during the flow cell test. (b) Faradaic efficiency (FE) of CoN_4-PC as a function of the applied potential in 1.0 M KOH. (c) The variations in current density and Faradaic efficiency against time of CoN_4-PC during the long-term potentiostatic test with the potential kept constant at 0.3 V. (d) Comparisons of H_2O_2 production rate and durability testing time period between CoN_4-PC and previously reported SACs in Table S6. (e) The degradation efficiency of the RhB organic dye over time. The inset shows the photos of the RhB solution after adding catholyte during degradation process.

equilibrium potentials (0.70 V and 1.23 V for the 2e$^-$ and 4e$^-$ pathways, respectively) of the CoN_4 and P_2-CoN_4 moieties are displayed in Fig. 5d and e, respectively. As shown in Fig. 5d, for the CoN_4 moiety, the last step of the transition from *OH to H_2O is the rate-determining step (RDS) for the 4e$^-$ pathway and the energy barrier is 0.33 eV. In comparison, the RDS for the 2e$^-$ pathway is the hydrogenation of the *OOH intermediate with a higher energy barrier of 0.36 eV, suggesting that the 4e$^-$ pathway is more energetically favored on the CoN_4 moiety. The situation is reversed in the case of the P_2-CoN_4 moiety, as shown in Fig. 5e. Specifically, for the 4e$^-$ pathway the hydrogenation of O_2 to form *OOH with an energy barrier of 0.44 eV is the RDS, while for the 2e$^-$ pathway it only requires 0.09 eV to overcome the energy barrier for transforming *OOH to H_2O_2, indicating that the 2e$^-$ pathway is preferred on the P_2-CoN_4 moiety and corroborating the results from electrochemical measurements.

4. Conclusion

In summary, we have developed a facile polymerization-pyrolysis approach to a high-performance electrocatalyst (CoN_4-PC) for H_2O_2 electrosynthesis consisting of atomically dispersed Co sites on N, P-codoped carbon substrate, which was characterized in detail by various techniques such as ADF-STEM, XRD, FT-IR, XPS, XANES and EXAFS. Combined experimental investigations and DFT calculations suggest that the introduction of P dopants in the form of C−P bonds can effectively induce the stretching of the Co−N bond of the CoN_4 moieties and

decrease the electron density of the Co atoms, leading to the optimization in the adsorption of the key intermediate (*OOH) on the active sites and thus promotion in the catalytic efficiency. Electrochemical measurements with RRDE and GDE configurations demonstrate the exceptional activity (E_{onset} = 0.81 V; TOF = 2.36 ± 0.15 s^{-1} at 0.65 V), selectivity (∼ 97%) and stability (110 h) of the CoN_4-PC catalyst, making it highly promising for practical large-scale H_2O_2 production. This work provides new insights into the electronic structure regulation of metal centers and structure–property relationship at the atomic level, which could be valuable to develop advanced catalysts for H_2O_2 production.

CRediT authorship contribution statement

Jingjing Liu, Zengxi Wei: Conceptualization, Investigation, Writing – original draft. **Zhichao Gong:** Data curation, Software. **Minmin Yan:** Methodology, Editing. **Yongfeng Hu:** Visualization, Investigation, Resources. **Shuangliang Zhao, Gonglan Ye, Huilong Fei:** Supervision, Funding acquisition, Writing – review & editing.

Declaration of Competing Interest

The authors declare that they have no known competing financial interests or personal relationships that could have appeared to influence the work reported in this paper.
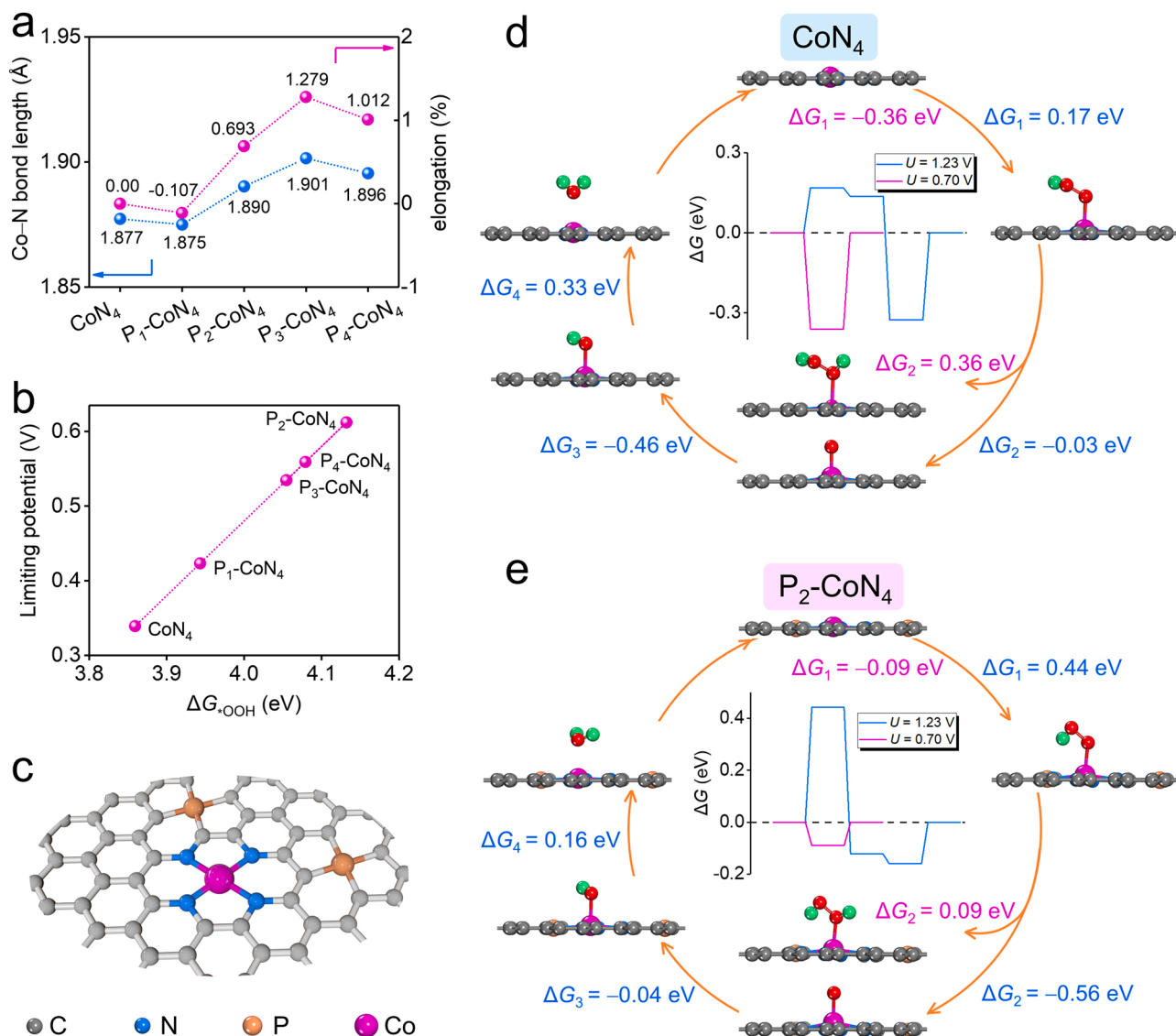
Fig. 5. DFT calculations. (a) Dependence of the mean bond length and elongation of Co−N bond in the CoN_4 moiety with different contents of P dopants, including CoN_4, P_1-CoN_4, P_2-CoN_4, P_3-CoN_4 and P_4-CoN_4. (b) Limiting potentials as a function of ΔG_{*OOH} for CoN_4, P_1-CoN_4, P_2-CoN_4, P_3-CoN_4 and P_4-CoN_4. (c) Optimized geometry (P_2-CoN_4) of CoN_4-PC with two PC_4 sites near the CoN_4 moiety. (d) ORR reaction pathways and free energy diagrams for the $2e^-$ and $4e^-$ ORR on the CoN_4 moiety. (e) ORR reaction pathways and free energy diagrams for the $2e^-$ and $4e^-$ ORR on the P_2-CoN_4 moiety. Green, grey, blue, red, caramel, and magenta spheres represent H, C, N, O, P and Co atoms, respectively.

Data availability

Data will be made available on request.

Acknowledgments

Declaration of Competing Interest

The authors declare no competing financial interest.

Appendix A. Supporting information

Supplementary data associated with this article can be found in the online version at doi:10.1016/j.apcatb.2022.122267.

References

[1] H.W. Kim, M.B. Ross, N. Kornienko, L. Zhang, J. Guo, P. Yang, B.D. McCloskey, Efficient hydrogen peroxide generation using reduced graphene oxide-based oxygen reduction electrocatalysts, Nat. Catal. 1 (2018) 282–290.

[2] Y. Xia, X. Zhao, C. Xia, Z.-Y. Wu, P. Zhu, J.Y.T. Kim, X. Bai, G. Gao, Y. Hu, J. Zhong, Y. Liu, H. Wang, Highly active and selective oxygen reduction to H_2O_2 on boron-doped carbon for high production rates, Nat. Commun. 12 (2021) 4225.

[3] Y. Sun, L. Han, P. Strasser, A comparative perspective of electrochemical and photochemical approaches for catalytic H_2O_2 production, Chem. Soc. Rev. 49 (2020) 6605–6631.

[4] https://www.imarcgroup.com/hydrogen-peroxide-technical-material-market-report.

[5] F. Sun, C. Yang, Z. Qu, W. Zhou, Y. Ding, J. Gao, G. Zhao, D. Xing, Y. Lu, Inexpensive activated coke electrocatalyst for high-efficiency hydrogen peroxide production: Coupling effects of amorphous carbon cluster and oxygen dopant, Appl. Catal. B: Environ. 286 (2021), 119860.

[6] P. Su, M. Zhou, X. Lu, W. Yang, G. Ren, J. Cai, Electrochemical catalytic mechanism of N-doped graphene for enhanced H_2O_2 yield and in-situ degradation of organic pollutant, Appl. Catal. B: Environ. 245 (2019) 583–595.

[7] S. Chen, T. Luo, X. Li, K. Chen, J. Fu, K. Liu, C. Cai, Q. Wang, H. Li, Y. Chen, C. Ma, L. Zhu, Y.R. Lu, T.S. Chan, M. Zhu, E. Cortes, M. Liu, Identification of the highly active Co-N_4 coordination motif for selective oxygen reduction to hydrogen peroxide, J. Am. Chem. Soc. 144 (2022) 14505.

[8] S. Chen, T. Luo, K. Chen, Y. Lin, J. Fu, K. Liu, C. Cai, Q. Wang, H. Li, X. Li, J. Hu, H. Li, M. Zhu, M. Liu, Chemical identification of catalytically active sites on oxygen-doped carbon nanosheet to decipher the high activity for electro-synthesis hydrogen peroxide, Angew. Chem. Int. Ed. 60 (2021) 16607–16614.

[9] Y. Bu, Y. Wang, G.F. Han, Y. Zhao, X. Ge, F. Li, Z. Zhang, Q. Zhong, J.B. Baek, Carbon-based electrocatalysts for efficient hydrogen peroxide production, Adv. Mater. 33 (2021) 2103266.

[10] B.-Q. Li, C.-X. Zhao, J.-N. Liu, Q. Zhang, Electrosynthesis of Hydrogen Peroxide Synergistically Catalyzed by Atomic Co-N_x-C Sites and Oxygen Functional Groups in Noble-Metal-Free Electrocatalysts, Adv. Mater. 31 (2019) 1808173.

[11] J.S. Jirkovsky, I. Panas, E. Ahlberg, M. Halasa, S. Romani, D.J. Schiffrin, Single atom hot-spots at Au-Pd nanoalloys for electrocatalytic H_2O_2 production, J. Am. Chem. Soc. 133 (2011) 19432–19441.

[12] A. Verdaguer-Casadevall, D. Deiana, M. Karamad, S. Siahrostami, P. Malacrida, T. W. Hansen, J. Rossmeisl, I. Chorkendorff, I.E. Stephens, Trends in the electrochemical synthesis of H_2O_2: enhancing activity and selectivity by electrocatalytic site engineering, Nano Lett. 14 (2014) 1603–1608.

[13] S. Yang, J. Kim, Y.J. Tak, A. Soon, H. Lee, Single-Atom Catalyst of Platinum Supported on Titanium Nitride for Selective Electrochemical Reactions, Angew. Chem. Int. Ed. 55 (2016) 2058–2062.

[14] S. Siahrostami, A. Verdaguer-Casadevall, M. Karamad, D. Deiana, P. Malacrida, B. Wickman, M. Escudero-Escribano, E.A. Paoli, R. Frydendal, T.W. Hansen, I. Chorkendorff, I.E. Stephens, J. Rossmeisl, Enabling direct H_2O_2 production through rational electrocatalyst design, Nat. Mater. 12 (2013) 1137–1143.

[15] Y. Wang, G.I.N. Waterhouse, L. Shang, T. Zhang, Electrocatalytic oxygen reduction to hydrogen peroxide: from homogeneous to heterogenous electrocatalysis, Adv. Energy Mater. 11 (2020) 2003125.

[16] Y. Wang, R. Shi, L. Shang, L. Peng, D. Chu, Z. Han, G.I.N. Waterhouse, R. Zhang, T. Zhang, Vertical graphene array for efficient electrocatalytic reduction of oxygen to hydrogen peroxide, Nano Energy 96 (2022), 107046.

[17] Y. Wang, Z. Zhang, X. Zhang, Y. Yuan, Z. Jiang, H. Zheng, Y.-G. Wang, H. Zhou, Y. Liang, Theory-driven design of electrocatalysts for the two-electron oxygen reduction reaction based on dispersed metal phthalocyanines, CCS Chem. 3 (2021) 585–593.

[18] M. Dan, R. Zhong, S. Hu, H. Wu, Y. Zhou, Z.-Q. Liu, Strategies and challenges on selective electrochemical hydrogen peroxide production: Catalyst and reaction medium design, Chem. Catal. 2 (2022) 1.

[19] J. Liu, Z. Gong, M. Yan, G. He, H. Gong, G. Ye, H. Fei, Electronic structure regulation of single-atom catalysts for electrochemical oxygen reduction to H_2O_2, Small 18 (2022) 2103824.

[20] G. He, M. Yan, H. Gong, H. Fei, S. Wang, Ultrafast synthetic strategies under extreme heating conditions toward single-atom catalysts, Int. J. Extrem. Manuf. 4 (2022), 032003.

[21] C. Tang, L. Chen, H. Li, L. Li, Y. Jiao, Y. Zheng, H. Xu, K. Davey, S.-Z. Qiao, Tailoring acidic oxygen reduction selectivity on single-atom catalysts via modification of first and second coordination spheres, J. Am. Chem. Soc. 143 (2021) 7819–7827.

[22] Q. Yang, W. Xu, S. Gong, G. Zheng, Z. Tian, Y. Wen, L. Peng, L. Zhang, Z. Lu, L. Chen, Atomically dispersed Lewis acid sites boost 2-electron oxygen reduction activity of carbon-based catalysts, Nat. Commun. 11 (2020) 5478.

[23] Z. Lin, Q. Zhang, J. Pan, C. Tsounis, A.A. Esmailpour, S. Xi, H.-Y. Yang, Z. Han, J. Yun, R. Amal, X. Lu, Atomic Co decorated free-standing graphene electrode assembly for efficient hydrogen peroxide production in acid, Energy Environ. Sci. 15 (2022) 1172.

[24] H. Fei, J. Dong, Y. Feng, C. Allen, C. Wan, B. Volosskiy, M. Li, Z. Zhao, Y. Wang, H. Sun, P. An, W. Chen, Z. Guo, C. Lee, D. Chen, I. Shakir, M. Liu, T. Hu, Y. Li, A. I. Kirkland, X. Duan, Y. Huang, General synthesis and definitive structural identification of MN_4C_4 single-atom catalysts with tunable electrocatalytic activities, Nat. Catal. 1 (2018) 63–72.

[25] T. He, Y. Chen, Q. Liu, B. Lu, X. Song, H. Liu, M. Liu, Y.-N. Liu, Y. Zhang, X. Ouyang, S. Chen, Theory-Guided Regulation of FeN_4 Spin State by Neighboring Cu Atoms for Enhanced Oxygen Reduction Electrocatalysis in Flexible Metal-Air Batteries, Angew. Chem. Int. Ed. 61 (2022) 202201007.

[26] X. Sun, Y. Tuo, C. Ye, C. Chen, Q. Lu, G. Li, P. Jiang, S. Chen, P. Zhu, M. Ma, J. Zhang, J.H. Bitter, D. Wang, Y. Li, Phosphorus Induced Electron Localization of Single Iron Sites for Boosted CO_2 Electroreduction Reaction, Angew. Chem. Int. Ed. 60 (2021) 23614–23618.

[27] J. Gao, H. Yang, X. Huang, S.-F. Hung, W. Cai, C. Jia, S. Miao, H.-M. Chen, X. Yang, Y. Huang, T. Zhang, B. Liu, Enabling Direct H_2O_2 Production in Acidic Media through Rational Design of Transition Metal Single Atom Catalyst, Chem 6 (2020) 658–674.

[28] H. Fei, J. Dong, D. Chen, T. Hu, X. Duan, I. Shakir, Y. Huang, X. Duan, Single atom electrocatalysts supported on graphene or graphene-like carbons, Chem. Soc. Rev. 48 (2019) 5207–5241.

[29] W. Yan, J. Sun, T. Hu, S. Tian, J. Feng, Y. Xiong, Significant boosting effect of single atom Pt towards the ultrasonic generation of H_2O_2: A two-way catalytic mechanism, Appl. Catal. B: Environ. 323 (2023), 122143.

[30] Y. Sun, L. Silvioli, N.R. Sahraie, W. Ju, J. Li, A. Zitolo, S. Li, A. Bagger, L. Arnarson, X. Wang, T. Moeller, D. Bernsmeier, J. Rossmeisl, F. Jaouen, P. Strasser, Activity-Selectivity Trends in the Electrochemical Production of Hydrogen Peroxide over Single-Site Metal-Nitrogen-Carbon Catalysts, J. Am. Chem. Soc. 141 (2019) 12372–12381.

[31] E. Jung, H. Shin, B.H. Lee, V. Efremov, S. Lee, H.S. Lee, J. Kim, W. Hooch Antink, S. Park, K.S. Lee, S.P. Cho, J.S. Yoo, Y.E. Sung, T. Hyeon, Atomic-level tuning of Co-N-C catalyst for high-performance electrochemical H_2O_2 production, Nat. Mater. 19 (2020) 436–442.

[32] H. Gong, Z. Wei, Z. Gong, J. Liu, G. Ye, M. Yan, J. Dong, C. Allen, J. Liu, K. Huang, R. Liu, G. He, S. Zhao, H. Fei, Low-Coordinated Co-N-C on Oxygenated Graphene for Efficient Electrocatalytic H_2O_2 Production, Adv. Funct. Mater. 32 (2021) 2106886.

[33] J. Yang, Z. Wang, C.X. Huang, Y. Zhang, Q. Zhang, C. Chen, J. Du, X. Zhou, Y. Zhang, H. Zhou, L. Wang, X. Zheng, L. Gu, L.M. Yang, Y. Wu, Compressive Strain Modulation of Single Iron Sites on Helical Carbon Support Boosts Electrocatalytic Oxygen Reduction, Angew. Chem. Int. Ed. 60 (2021) 22722–22728.

[34] Q. Wang, Q. Feng, Y. Lei, S. Tang, L. Xu, Y. Xiong, G. Fang, Y. Wang, P. Yang, J. Liu, W. Liu, X. Xiong, Quasi-solid-state Zn-air batteries with an atomically dispersed cobalt electrocatalyst and organohydrogel electrolyte, Nat. Commun. 13 (2022) 3689.

[35] X. Yang, Y. Wang, X. Tong, N. Yang, Strain Engineering in Electrocatalysts: Fundamentals, Progress, and Perspectives, Adv. Energy Mater. 12 (2021) 2102261.

[36] G. Han, X. Zhang, W. Liu, Q. Zhang, Z. Wang, J. Cheng, T. Yao, L. Gu, C. Du, Y. Gao, G. Yin, Substrate strain tunes operando geometric distortion and oxygen reduction activity of CuN_2C_2 single-atom sites, Nat. Commun. 12 (2021) 6335.

[37] J. Qin, H. Liu, P. Zou, R. Zhang, C. Wang, H.L. Xin, Altering ligand fields in single-atom sites through second-shell anion modulation boosts the oxygen reduction reaction, J. Am. Chem. Soc. 144 (2022) 2197–2207.

[38] T. He, W. Wang, F. Shi, X. Yang, X. Li, J. Wu, Y. Yin, M. Jin, Mastering the surface strain of platinum catalysts for efficient electrocatalysis, Nature 598 (2021) 76–81.

[39] W. Peng, J. Han, Y.R. Lu, M. Luo, T.-S. Chan, M. Peng, Y. Tan, A General Strategy for Engineering Single-Metal Sites on 3D Porous N, P Co-Doped $Ti_3C_2T_X$ MXene, ACS Nano 16 (2022) 4116–4125.

[40] Y.J. Sa, J.H. Kim, S.H. Joo, Active edge-site-rich carbon nanocatalysts with enhanced electron transfer for efficient electrochemical hydrogen peroxide production, Angew. Chem. Int. Ed. 58 (2019) 1100–1105.

[41] K. Yuan, D. Lutzenkirchen-Hecht, L. Li, L. Shuai, Y. Li, R. Cao, M. Qiu, X. Zhuang, M.K.H. Leung, Y. Chen, U. Scherf, Boosting oxygen reduction of single iron active sites via geometric and electronic engineering: nitrogen and phosphorus dual coordination, J. Am. Chem. Soc. 142 (2020) 2404–2412.

[42] H. Yin, P. Yuan, B.-A. Lu, H. Xia, K. Guo, G. Yang, Q. Qu, D. Xue, Y. Hu, J. Cheng, S. Mu, J.-N. Zhang, Phosphorus-Driven Electron Delocalization on Edge-Type FeN_4 Active Sites for Oxygen Reduction in Acid Medium, ACS Catal. 11 (2021) 12754–12762.

[43] K. Li, S. Zhang, X. Zhang, S. Liu, H. Jiang, T. Jiang, C. Shen, Y. Yu, W. Chen, Atomic Tuning of Single-Atom Fe-N-C Catalysts with Phosphorus for Robust Electrochemical CO_2 Reduction, Nano Lett. 22 (2022) 1557.

[44] J. Zhang, Z. Zhao, Z. Xia, L. Dai, A metal-free bifunctional electrocatalyst for oxygen reduction and oxygen evolution reactions, Nat. Nanotechnol. 10 (2015) 444–452.

[45] J. Liu, T. He, Q. Wang, Z. Zhou, Y. Zhang, H. Wu, Q. Li, J. Zheng, Z. Sun, Y. Lei, J. Ma, Y. Zhang, Confining ultrasmall bimetallic alloys in porous N-carbon for use as scalable and sustainable electrocatalysts for rechargeable Zn-air batteries, J. Mater. Chem. A. 7 (2019) 12451–12456.

[46] X. Fan, Y. Zhou, X. Jin, R.B. Song, Z. Li, Q. Zhang, Carbon material-based anodes in the microbial fuel cells, Carbon, Energy 3 (2021) 449–472.

[47] J. Liu, Z. Gong, C. Allen, W. Ge, H. Gong, J. Liao, J. Liu, K. Huang, M. Yan, R. Liu, G. He, J. Dong, G. Ye, H. Fei, Edge-hosted Fe-N_3 sites on a multiscale porous carbon framework combining high intrinsic activity with efficient mass transport for oxygen reduction, Chem. Catal. 1 (2021) 1291–1307.

[48] K.N. Kudin, B. Ozbas, H.C. Schniepp, R.K. Prud'homme, I.A. Aksay, R. Car, Raman Spectra of Graphite Oxide and Functionalized Graphene Sheets, Nano Lett. 8 (2008) 36–41.

[49] J.E. Proctor, E. Gregoryanz, K.S. Novoselov, M. Lotya, J.N. Coleman, M.P. Halsall, High-pressure Raman spectroscopy of graphene, Phys. Rev. B 80 (2009), 073408.

[50] P. Chen, N. Zhang, S. Wang, T. Zhou, Y. Tong, C. Ao, W. Yan, L. Zhang, W. Chu, C. Wu, Y. Xie, Interfacial engineering of cobalt sulfide/graphene hybrids for highly efficient ammonia electrosynthesis, Proc. Natl. Acad. Sci. 116 (2019) 6635–6640.

[51] Y. Zhao, N. Yang, H. Yao, D. Liu, L. Song, J. Zhu, S. Li, L. Gu, K. Lin, D. Wang, Stereodefined Codoping of sp-N and S Atoms in Few-Layer Graphdiyne for Oxygen Evolution Reaction, J. Am. Chem. Soc. 141 (2019) 7240–7244.

[52] S. Ji, B. Jiang, H. Hao, Y. Chen, J. Dong, Y. Mao, Z. Zhang, R. Gao, W. Chen, R. Zhang, Q. Liang, H. Li, S. Liu, Y. Wang, Q. Zhang, L. Gu, D. Duan, M. Liang, D. Wang, X. Yan, Y. Li, Matching the kinetics of natural enzymes with a single-atom iron nanozyme, Nat. Catal. 4 (2021) 407–417.

[53] Y. Wang, K. Liu, J. Li, X. Yang, J. Hu, T.-S. Chan, X. Qiu, W. Li, M. Liu, CoN_4 active sites in locally distorted carbon structure for efficient oxygen reduction reaction via regulating coordination environment, Chem. Eng. J. 429 (2022), 132119.

[54] P. Cao, X. Quan, K. Zhao, X. Zhao, S. Chen, H. Yu, Durable and Selective Electrochemical H_2O_2 Synthesis under a Large Current Enabled by the Cathode with Highly Hydrophobic Three-Phase Architecture, ACS Catal. 11 (2021) 13797–13808.

[55] H. Sheng, A.N. Janes, R.D. Ross, D. Kaiman, J. Huang, B. Song, J.R. Schmidt, S. Jin, Stable and selective electrosynthesis of hydrogen peroxide and the electro-Fenton process on $CoSe_2$ polymorph catalysts, Energy Environ. Sci. 13 (2020) 4189–4203.

[56] C. Liu, H. Li, J. Chen, Z. Yu, Q. Ru, S. Li, G. Henkelman, L. Wei, Y. Chen, 3d transition-metal-mediated columbite nanocatalysts for decentralized electrosynthesis of hydrogen peroxide, Small 17 (2021) 2007249.

[57] S. Wang, X. Zhang, G. Chen, B. Liu, H. Li, J. Hu, J. Fu, M. Liu, Hydroxyl radical induced from hydrogen peroxide by cobalt manganese oxides for ciprofloxacin degradation, Chin. Chem. Lett. 33 (2022) 5208–5212.

[58] Y. Yu, M. Pan, J. Peng, D. Hu, Y. Hao, Z. Qian, A review on recent advances in hydrogen peroxide electrochemical sensors for applications in cell detection, Chin. Chem. Lett. 33 (2022) 4133–4145.